

Article

Structural Dynamic Improvement for Petal-Type Deployable Solid-Surface Reflector Based on Numerical Parameter Study

He Huang * , Qiang Cheng and Lei Zheng

School of Mechanics, Civil Engineering and Architecture, Northwestern Polytechnical University, Xi'an 710072, China; cheng_qiang@mail.nwpu.edu.cn (Q.C.); zyfl@mail.nwpu.edu.cn (L.Z.)

* Correspondence: hehuang0623@nwpu.edu.cn; Tel.: +86-13-6566-76823

Received: 21 August 2020; Accepted: 18 September 2020; Published: 20 September 2020



Featured Application: This article can be applied to deployable reflector antennas in aerospace engineering.

Abstract: Petal-type Deployable Solid-surface Reflector (PDSR) is a kind of important structure widely applied in deployable reflector antennas in aerospace engineering. The dynamic properties of this reflector structure in deployed state are significant to the reflector accuracy for antennas. However, the study of the dynamic evaluation of deployable structure with revolute joints is difficult and seldom concerned by researchers. In order to study dynamic properties of the PDSR, the Cable Replacement Method (CRM) was utilized to equivalently simulate the nonlinear structural stiffness of the revolute joint for numerical analyses. The Finite Element Model (FEM) of this reflector structure was established by commercial software ANSYS (ANSYS Inc., Canonsburg, PA, USA) and verified by the theoretical analysis and dynamic test of actual prototype model. The natural frequencies and mode shapes of deployed reflector were computed to study the influence of drag spring design parameters as stiffness, pre-tensioned force, and distance of two adjacent linkage butts. Finally, the analysis results were concluded that the drag springs between two adjacent petals can essentially improve the dynamic performance of reflector structure in deployed state. It can be a useful technical system for future engineering applications of PDSR antennas.

Keywords: solid surface; deployable reflector; reflector antenna; dynamic property; revolute joint; natural frequency

1. Introduction

Deployable structures have been widely applied to the aerospace industry [1–3], such as aperture antennas [4–8], solar arrays [9,10], space masts [11,12], and so on. One of the most important advantages is the perfect package property [13] of deployable structures so as to store in the fairing of launch vehicle and deploy into structures in orbit. This way can enormously reduce the weight and enlarge the size of these pay-load structures. However, the stiffness and dynamic properties of structures are greatly decreased along with the weight reduction and size expansion [14,15]. Therefore, the improvement of dynamic properties is an essential study on deployable structures in working state for the further applications.

Different with common structures, the deployable structure generally has the drastically structural transformations from folded state to deployed state [13]. In order to fulfill this function, the deployable mechanism is necessarily employed by segmented bodies, kinematic pairs, and driving devices. These components may damage the structural integrity or lead to the nonlinear response and weaken

structures [16,17]. Thus, the accurate evaluation of dynamic properties is a significant but difficult part to study deployable structures in work state.

Previous studies on dynamic properties of deployable structures have mainly focused on simplified models. Weeks [18] developed a simplified mathematical model of a NASA solar array flight experiment configuration to investigate the free vibration and force-response behavior by the Galerkin method for the truncated set of second-order differential equations. Yan et al. [16] conducted the experiment of a deployable truss structure to explore the effects of joints on structural dynamics. The results reflected the complex nonlinear dynamic behavior and reduction of dynamic performances. Li et al. [19] established the FEM of an experimental deployable truss structure with considering the clearance joint by ANSYS to study the transient dynamic analysis based on a virtual experimental model analysis method. Guo et al. [17] developed a cantilever beam model containing linear joints based on FEM to analyze the influence of joint on natural frequencies and mode shapes. It was shown that nonlinear effects of free play and hysteresis lead dynamic responses switch from one resonance frequency to another when the amplitude exceed demarcation values. Liu et al. [20] proposed an optimization method with a dynamic constraint for the maximum stiffness/mass ratio to develop a new large cable-rib deployable antenna. These studies explore the dynamic properties of deployable structures in order to deeply develop the applications. Because these deployable structures on the satellites suffer from the vibrations, especially during the satellite attitude adjustment, the flexibility of deployed structures may bring trouble for the dynamic controls.

However, research about the structural dynamics seldom pays attention to deployable solid-surface reflector antennas. Thereinto, the Petal-type Deployable Solid-surface Reflector (PDSR) has been widely utilized in the aerospace applications [13,21–24]. The parabolic reflector is generally divided into the central hub and several petals with the connections by the deploying mechanism. The deploying mechanism can fulfill the petal deploying from folded state to deployed state; meanwhile, it may also bring about the unstableness [13]. In regard to not only the deploying process but also the deployed state, the dynamic properties should be paid attention to for the stability of reflector surface accuracy [25,26]. Especially in deployed working state, the reflector structure showing apparent flexibility may cause the flexible vibration or the resonance with the satellite.

Therefore, for this paper, a PDSR in deployed state was modeled to deeply explore its structural dynamic properties. The design of this reflector is presented in detail below. Then, the FEM was established by commercial software ANSYS. Thereinto, a kind of Cable Replacement Method (CRM) was employed here to equivalently simulate the structural stiffness of the revolute joint. The model was verified by theoretical equation based on the Rayleigh Method and the full-mode vibration excitation test for actual prototype model. The natural frequencies and mode shapes of deployed reflector were compared to study the influence of design parameters. Several conclusions were obtained in the end.

2. Model Design and Details

For a kind of PDSR utilized in a cubic microsatellite, the main components are the central hub, petals, supporting bars, linkage butts, and drag springs as shown in Figure 1 [13]. The parabolic surface is divided into a central hub and several identical parabolic petals around the central hub. These divided segments aim to maintain the parabolic profile as a reflector.

Each petal is connected to the central hub by a supporting bar with two revolute joints on the two ends. The joint between the central hub and supporting bar is set along the circumferential direction of hub, while the joint between the petal and supporting bar is set along the radial direction of petal. These two single-direction joints are orthogonal to fulfill the petal deployment mechanism with the specific rotation angle combinations. The torsion spring is installed in each single-direction pin to provide the driving torque for petal deployment. The rotation limiter in each joint is designed to make a restriction of rotation angle and passively lock the structure in deployed state. The design parameters of reflector surface are defined in Cartesian coordinate system O-XYZ shown in Figure 1c. The vertex of the central hub is located at the coordinate origin O.

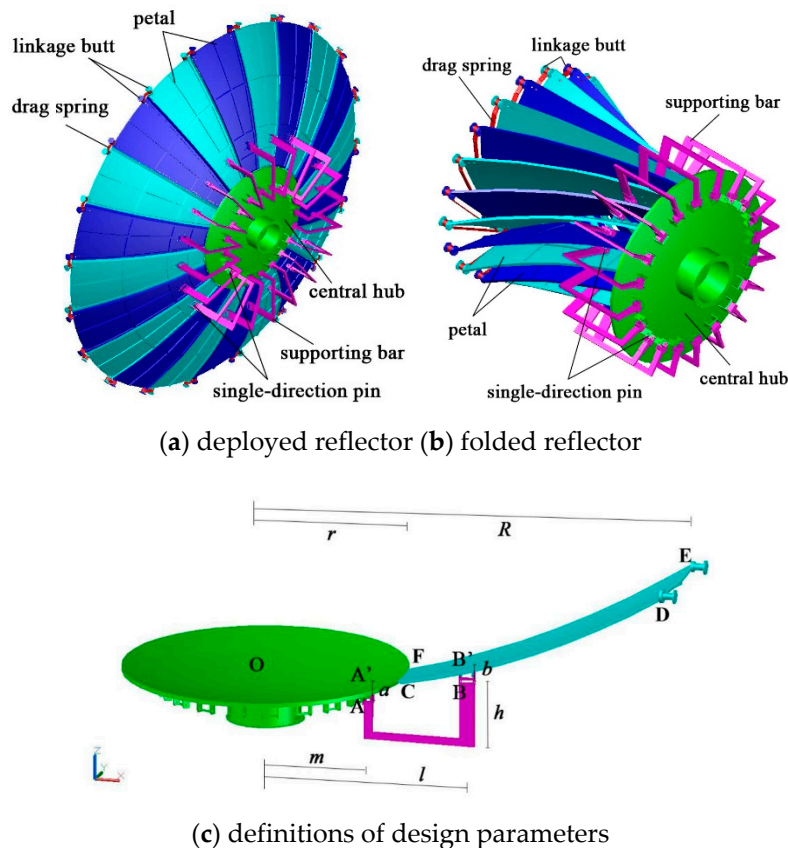


Figure 1. Schematic diagram of Petal-type Deployable Solid-surface Reflector (PDSR) model.

A kind of 1200 mm aperture PDSR is employed here as a specific object to study its structural dynamic properties for the future application to microsattellites. The focal length of antenna is $f = 480$ mm and the focus-diameter-ratio is defined as $\lambda = 0.4$. The parabolic reflector surface equation is expressed as $x^2 + y^2 = 1920z$. The curved Surface CDFE shown in Figure 1 is the main reference petal that is symmetrical along the Plane XOZ. The projection radius of the central hub on the Plane XOY is r , while the projection radius of the reference petal on the Plane XOY is $[r, R]$, where $r = 200$ mm, $R = 600$ mm. The pins of two orthogonal revolute joints are, respectively, defined as pin A and B. The rotation angles are defined as $\omega = -90^\circ$ and $\theta = 60^\circ$ along pin A and B, respectively. The horizontal distances from point A and point B to the vertex of central hub are defined as $m = 150$ mm, $l = 300$ mm. The vertical distances from pin A and pin B to the parabolic surface are both defined as $a = b = 15$ mm, respectively.

Based on the models in Reference [13], two linkage butts are installed on the top of each petal as shown in Figure 2a. For each of the two adjacent petals, the adjacent linkage butts are linked by the drag spring. The drag spring is tensioned with storing the elastic potential energy when the structure is folded. As soon as the folded structure is unlocked to deploy, the drag spring quickly shortens to drag the adjacent linkage butts together. Finally, in totally deployed state, the drag spring still has the tension stress to keep petals stably locked. The deploying processes of the two models were conducted by ADAMS software simulations in Reference [13]. In view of its simulation results, it was indicated that the drag springs set on linkage butts can improve the integrality and stability of antenna during the deploying. Nevertheless, the function of drag springs was re-examined to deeply explore the structural dynamic properties of this PDSR in deployed state.

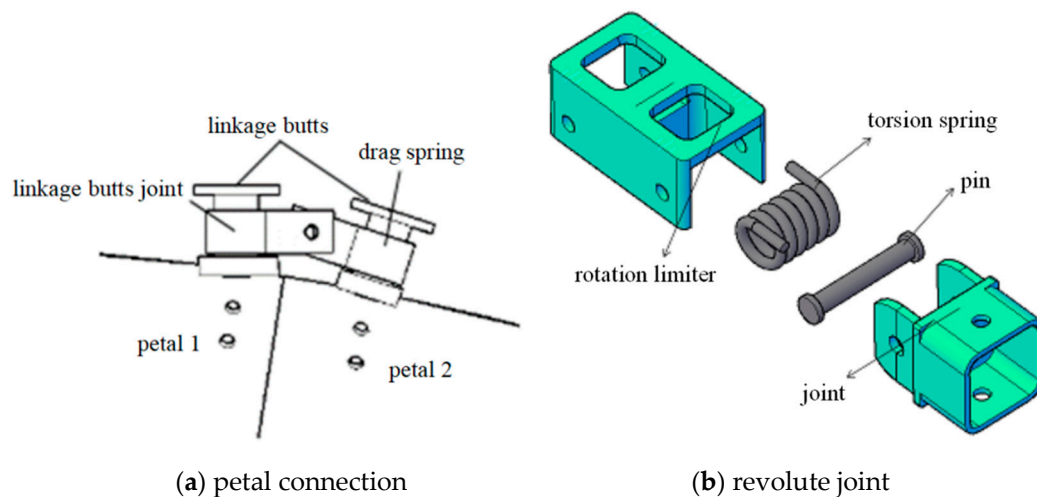


Figure 2. Schematic diagram of model details.

The weakest parts of the deployed reflector should be the revolute joints in the structural dynamic analysis. The stiffness in each revolute joint of the PDSR is mainly provided by the torsion spring and the rotation limiter. The details of typical revolute joint are shown in Figure 2b [27]. The joint is vertically folded with the twisted torsion spring retaining elastic potential energy and then rotates counterclockwise around the pin axis during deploying. After rotating to horizontal configuration, the joint is restricted by the rotation limiter from rotating. At this time, the residual torque of the torsion spring and the contact force of rotation limiter lock this revolute joint up as an entire component. Therefore, the connection mode of revolute joint is changed between a hinge and an elastic component. The stiffness in the revolute joint shows a kind of nonlinear variation based on different level of the residual torque in the torsion spring. Thus, the works of definition and simulation for the revolute joint is the key to the accurate results.

3. Analysis Models by CRM

As mentioned above, in order to deeply explore the dynamic properties of the PDSR affected by drag springs in deployed state, FEMs are established on the basis of commercial software ANSYS. At the same time, the CRM is utilized to implement the model analyses so as to deal with the nonlinear problem for the stiffness definition of torsion springs in revolute joints.

3.1. ANSYS Modeling

To study the dynamic properties of the deployed reflector structure in orbit, the FEMs are established here. The typical materials widely used in aerospace engineering are listed in Table 1 with their mechanical parameters. The central hub, supporting bars, and petals use a kind of polymer composite material. The satellite interface and cables in cable replacement modeling method are made of aluminum alloy, while the joint pins are made of titanium alloy. Based on ANSYS modeling in Figure 3, the details of element information for each component are listed in Table 2. The element mesh of model is made as shown in Figure 3, considering the computing efficiency and accuracy. The shell element mesh size is reduced at the connection with other components to develop the local accuracy.

Table 1. Material parameters.

Material	Elastic Modulus (GPa)	Poisson's Ratio	Density (kg/mm ³)
Aluminum alloy	70	0.33	2.7×10^{-6}
Polymer composite material	120	0.3	1.7×10^{-6}
Titanium alloy	108	0.34	4.5×10^{-6}

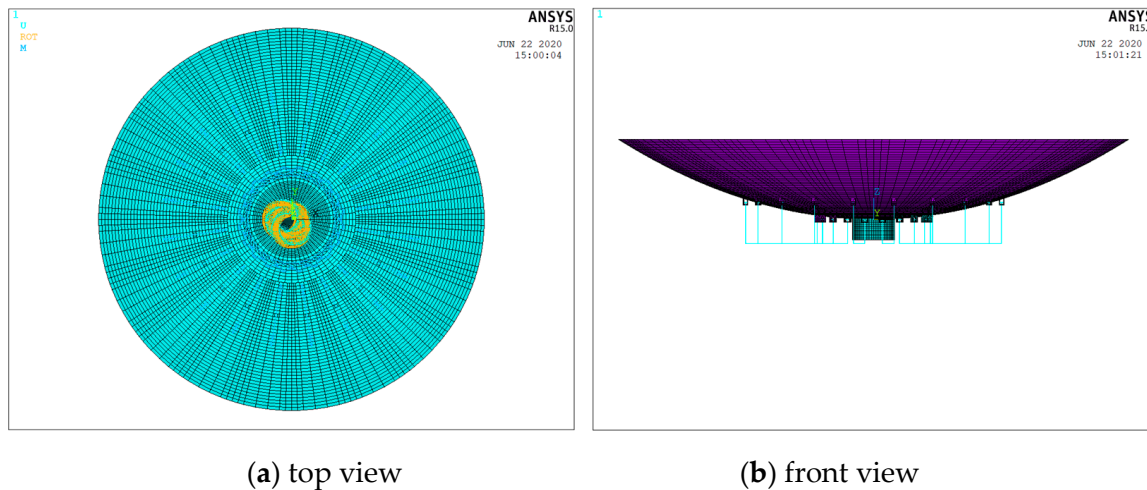


Figure 3. ANSYS model without drag springs.

Table 2. Elements and real constants.

Component	Element	Real Constant
Satellite interface	Shell63	Thickness 6 mm
Central hub & petals	Shell63	Thickness 1 mm
Joint plates & rotation limiters	Shell63	Thickness 1.5 mm
Cables	Link10	Area 6 mm ²
Pins	Beam188	Circular section, diameter 3.5 mm
Supporting bars	Beam188	Rectangular tube section, 22 mm × 5 mm, thickness 1.2 mm
Linkage butts	Beam188	Circular section, diameter 11 mm
Torsion springs	Combin14	Stiffness 1.85 N·mm/°
Drag springs	Combin14	Stiffness 0.4 N·mm

The drag spring is connected with two adjacent petals through linkage butts at the end of each petal shown Figure 2a. Each linkage butt modeled as listed in Table 2 is fixed on the edge of the petal. The drag spring is established as a linear spring fixed on the end of two adjacent linkage butt with a pair of pre-tensioned forces $T = 3.5 \text{ N}$. The FEM with drag springs is shown in Figure 4.

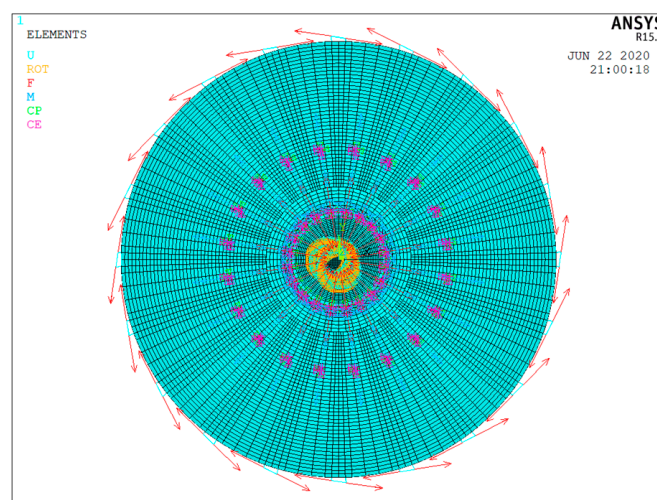


Figure 4. ANSYS model with drag springs.

3.2. CRM for Revolute Joint Modeling

In order to effectively simulate the nonlinear structural model of this revolute joint, the CRM is employed here in the dynamic analysis by ANSYS. The fundamental thought of this method is to use a

cable element instead of the contact between the joint and rotation limiter. It is also assumed that the influence of joint clearance is ignored in the modal analysis.

For the modal analysis in deployed state, the contact force between the joint and rotation limiter actually provides the contact stiffness, if there is a counterclockwise rotation trend. On the contrary, only the torsion spring with residual torque provides the stiffness for the joint, if the joint is separated from the rotation limiter and rotates around the opposite direction. This situation is very similar to the cable element that can only suffer tensions but no compressions. Therefore, the cable element with the pre-tensioned force can equivalently simulate the contact stiffness and the invalid condition between the joint and rotation limiter.

The details of revolute joint around the pin between the rotation limiter and supporting bar is shown in Figure 5 on the basis of cable replacement modeling method. Point 1 and 2 of the pin are fixed on the node of two plates, respectively, on the two sides with only releasing the rotation degree of freedom (DOF) around the pin axis. The node on the end of supporting bar and the node on the intersection point of the pin are coupled together with sharing the same DOFs. Point 3 connects the node on top face of the rotation limiter with the node on one end of cable by sharing the same translation DOFs. The other end of the cable on Point 4 is coupled with the node of supporting bar on point 5 by also sharing the same translation DOFs. Hence, the cable links the supporting bar with the rotation limiter to replace the contact stiffness between them.

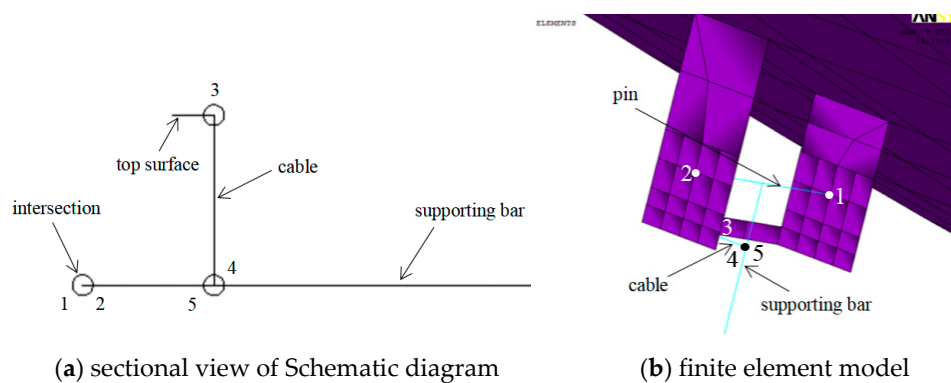


Figure 5. Modeling details of revolute joint.

3.3. Model Parameter Combinations

In order to fully explore the factors that affect the dynamic properties of this PDSR in deployed state, several design parameters about the drag spring, such as the stiffness, the pre-tensioned force, and the distance of linkage butts, are taken into consideration. The groups of different parameter combinations are organized in Table 3 on the foundation of single variable principle.

Table 3. Combinations of different parameters.

No.	Drag Spring	Stiffness S (N/m)	Pre-Tensioned Force P (N)	Distance of Linkage Butts L (mm)
1	with	0.4	3.5	40
2	without	-	-	-
3	with	40	3.5	40
4	with	4.0	3.5	40
5	with	4×10^{-4}	3.5	40
6	with	4×10^{-7}	3.5	40
7	with	0.4	3.0	40
8	with	0.4	2.5	40
9	with	0.4	2.0	40
10	with	0.4	0	40
11	with	0.4	3.5	80
12	with	0.4	3.5	150

Thereinto, the original model without drag springs is Model 2, while the model with drag springs is Model 1. The comparison between Model 1 and 2 in following Section 5.1 explores the function of drag springs. The stiffness of drag spring S is chosen as 0.4 N/m, 40 N/m, 4.0 N/m, 4×10^{-4} N/m, and 4×10^{-7} N/m, respectively, in Model 1, 3, 4, 5, and 6 to make a comparison in Section 5.2. Similarly, the pre-tensioned force of drag spring P is defined as 3.5 N, 3.0 N, 2.5 N, 2.0 N, and 0, respectively in Model 1, 7, 8, 9, and 10 for discussing in Section 5.3. The distance of the ends of two adjacent linkage butts is chosen as 40 mm, 80 mm, and 150 mm, respectively, in Model 1, 11, and 12 in Section 5.4.

4. Model Verification

Before analyses, the numerical simulation by ANSYS is verified by the theoretical method and laboratory actual prototype model.

4.1. Theoretical Method

Firstly, the theoretical equation based on the Rayleigh Method [28] is utilized to verify the following numerical simulation. Each petal can be equivalent to a cantilever beam. On account of energy conservation principle, the approximate solution of frequency ω can be expressed as

$$\omega^2 = \frac{\int_r^R EI[Y''(x)]^2 ds + k_t[Y'(x)]^2 \Big|_{x=r}}{\int_r^R m[Y(x)]^2 ds}, \quad (1)$$

where the ds is integrated along the parabolic curve as $ds = (1 + z'^2)^{1/2} dx$. E is the elastic modulus shown in Table 1, while k_t is the stiffness of torsion spring shown in Table 2. The petal section moment of inertia is approximately defined as $I = (\pi/10) \cdot xt^3/12$, where t is the petal thickness listed in Table 2. The mass of each dx segment is defined as $m = \rho \pi xt / 10$, where ρ is the petal density listed in Table 1. The shape function $Y(x)$ is the undetermined function to approach the actual mode shape.

When the shape function is defined as $Y(x) = a x^2$, the equation can be rewritten as

$$\omega^2 = \frac{\frac{\pi t^3 E}{120} 4a^2 \int_r^R x \sqrt{1 + \left(\frac{x}{960}\right)^2} dx + 4a^2 k_t x^2 \Big|_{x=r}}{\frac{\rho \pi t}{10} a^2 \int_r^R x \sqrt{1 + \left(\frac{x}{960}\right)^2} x^4 dx}. \quad (2)$$

The first natural frequency is calculated as $\omega = 0.6863$ Hz. This result is basically assumed that the vibration firstly occurs in the petal because of its flexibility. Although it may have the error because of this evaluation method and equivalent assumptions for this complex structure, this result can generally assess the dynamic property of this kind of deployable petal-type reflector structure.

4.2. Prototype Model Test

Secondly, the actual prototype is fabricated as aforementioned design model with drag springs. It is tested by Dynamic Signal Test System DH8303 based on the full-mode vibration exciter method [29] by Jiangsu Donghua Test Technology Co. Ltd. Thereinto, the micro exciter has the maximum exciting force 100 N and the frequency range from 0.1 Hz to 1 kHz. The signal generator can provide all sorts of signal with the frequency range from 0.01 Hz to 10 kHz. The power amplifier has rated output power 200 W with the frequency range from direct current to 40 kHz. The micro exciter and sensors are set on the petals as shown in Figure 6. The sensors are located at two ends of the petal for acquisitions of vibration signal by the micro exciter from different excitation locations. Finally, the first six natural frequencies limited by the sensor and exciter number are obtained in Table 4 to make a comparison between the test and simulation for Model 1.

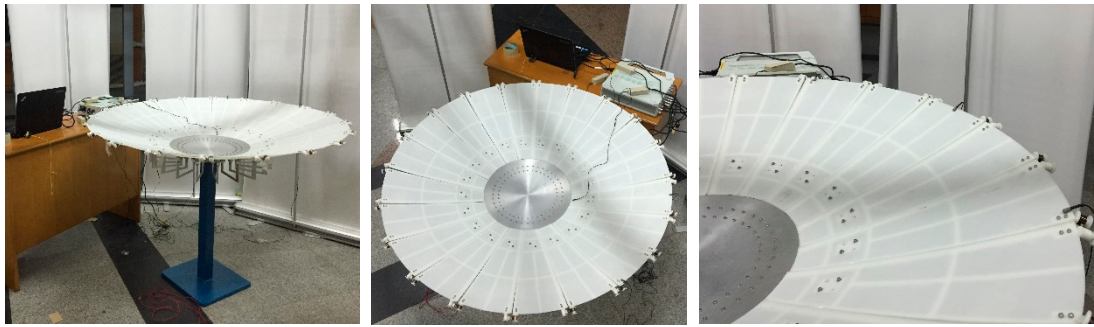


Figure 6. Test model by full-model vibration exciter method.

Table 4. Natural frequencies (Hz) of test and simulation for Model 1.

Frequency Order	Test	Simulation
1	0.8163	0.7847
2	0.8629	0.8301
3	0.8723	0.8533
4	0.9007	0.8819
5	0.9206	0.9268
6	0.9600	0.9858

From the results above, the first frequency results of test and simulation are close to the theoretical result and in the same level. It is reasonable that the theoretical result is little lower because it only concerns one petal without the effect of adjacent petals. The simulation almost coincides with test. For each frequency order, the relative error is less than 3.9%. These errors between the test and simulation in Table 4 may be caused by the test system and simulation model refinement.

The petal has the revolution DOF along the pin axis locked by the torsion spring and rotation limiter so that the structure is more flexible at the revolute joint than other components. In the test, the structure is hardly excited in a very lower frequency domain by the micro exciter so as to show that the test frequencies of first four orders are little bigger than the simulation frequencies in Table 4. Moreover, the exciter and sensors as the extra mass on the petal lead to enlarge the structural flexible as showing the smaller test frequencies of last two orders in Table 4. These two aspects together may be the main factors to slightly narrow down the lower frequency domain and lead to these errors in the test. But these errors are allowable, and the results are credible.

Therefore, it is stated that the simulation of CRM is practicable, and this numerical model is verified by both theoretical method and prototype model test for the following discussions.

5. Analysis Results

Based on the finite element analyses by ANSYS, the mode shapes and frequencies of these different models are obtained to discuss the effects of different parameters.

5.1. Effect of Drag Springs

This paper mainly studies about the effect of drag springs to improve the structural dynamics for this PDSR. According to the numerical simulations, the first ten natural vibration frequencies of Model 1 and 2 are listed in Table 5 and their mode shapes are shown in the Figure 7.

Table 5. Natural frequencies (Hz) of Mode 1 and 2.

Frequency Order	Model 1 with Drag Springs	Model 2 without Drag Springs
1	0.7847	0.3331
2	0.8301	0.3360
3	0.8533	0.3419
4	0.8819	0.3631
5	0.9268	0.7635
6	0.9858	1.2923
7	1.0077	1.2948
8	1.0359	3.8519
9	1.0896	3.8637
10	1.1364	3.8809

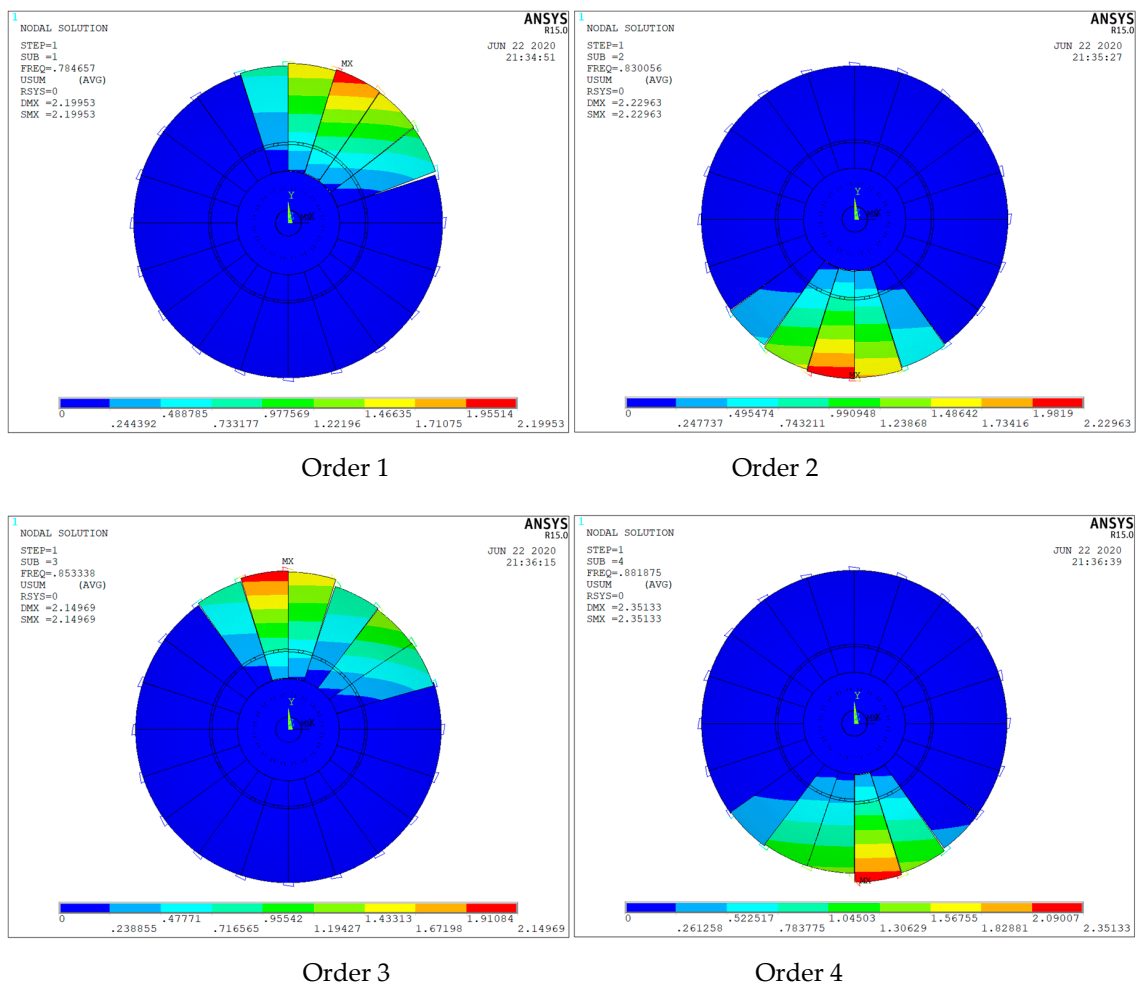
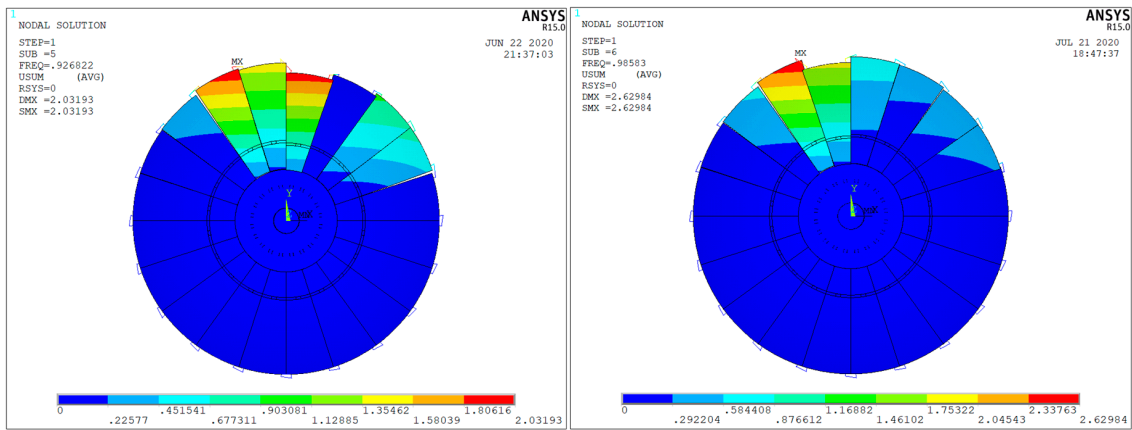
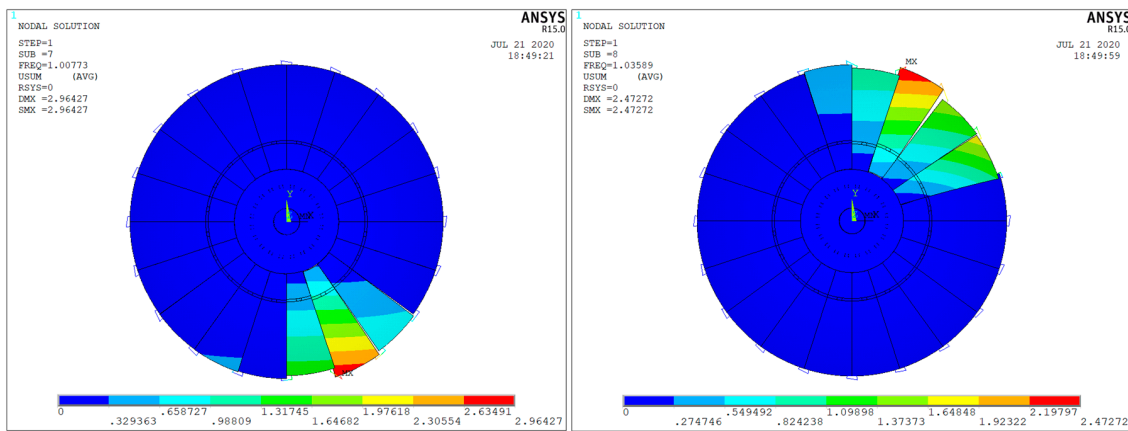


Figure 7. Cont.



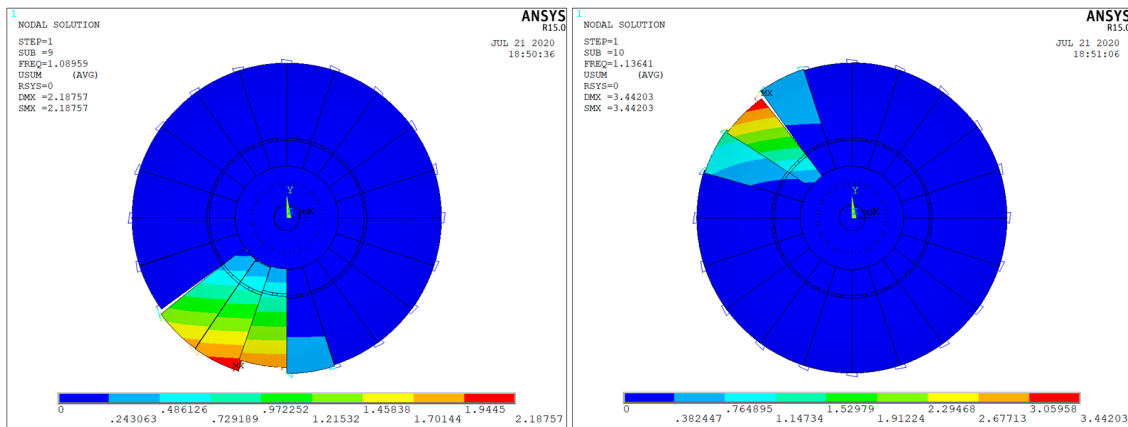
Order 5

Order 6



Order 7

Order 8



Order 9

Order 10

(a) Model 1 with drag springs

Figure 7. Cont.

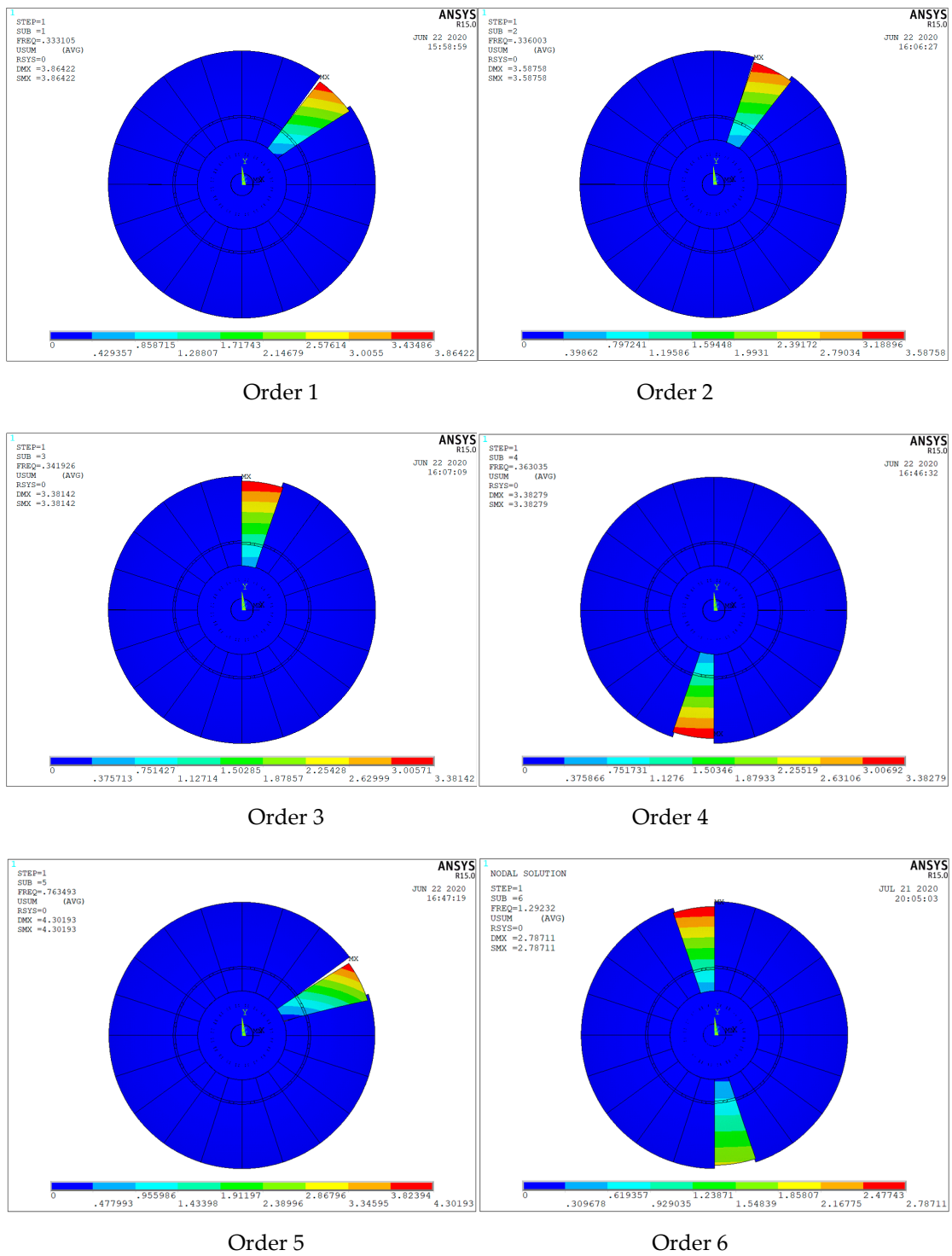


Figure 7. Cont.

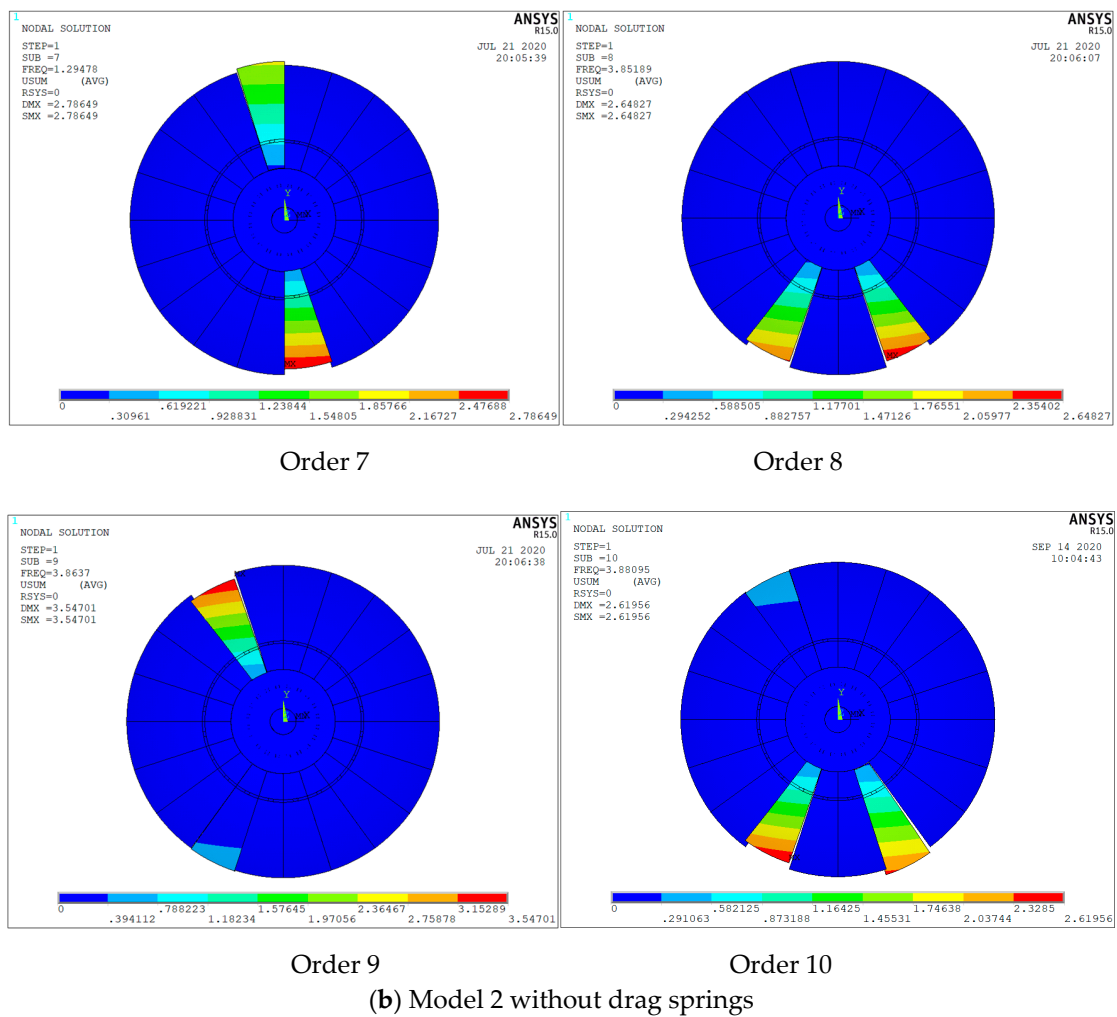
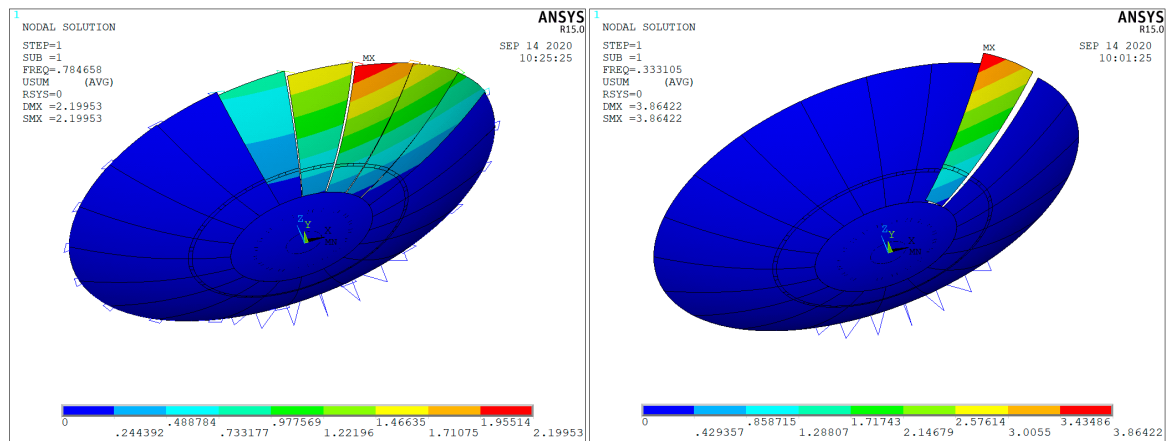


Figure 7. First ten mode shapes of the reflector.

In order to clearly illustrate the vibration mode, the first order mode shapes of Model 1 and 2 in 3D visualization are shown in Figure 8 as an example. It is shown that the petal vibration mode has the relationship with the deployment mechanism as Figure 1a,b. Because two orthogonal revolutes pins of the deployment mechanism are set by aforementioned CRM. The DOF of pin rotation is released and locked by the rotation limiter and the stiffness of torsion spring. Hence, it is demonstrated that the petal in Figure 8b easily occurs the upwarp with maximum displacement 3.86 mm as the first order mode shape, while the five petals connected with drag springs in Figure 8a have the smaller vibration with maximum displacement 2.20 mm. Other orders have the similar petal vibration mode.

For the mode shapes of Model 1 with the drag springs, several adjacent petals have the vibrations together in all ten modes in Figure 7a and the difference of these modes is the different petal combinations. The main reason is the function of drag spring by providing the tension stiffness between two adjacent petals. On the contrary, in Figure 7b, the mode shapes of Model 2 without drag springs are all the single-petal vibration. The first five orders of Model 2 are one single-petal vibration in different locations, and the last five orders are two single-petal vibration with different combinations.



(a) Model 1 with drag springs

(b) Model 2 without drag springs

Figure 8. First order mode shapes of Model 1 and 2 in 3D visualization.

From Table 5, the natural frequencies of the first five orders for Model 2 are much smaller than Model 1, while the rests of five frequencies for Model 2 are larger than Model 1. Combined with the difference of mode shapes for Model 1 and 2 in Figure 7, therefore, Model 2 has much more dispersed frequency domain and more flexible dynamic property in lower frequency domain. This performance is very averse to the reflector structure in deployed working state. Especially suffering from external disturbance, the model without drag springs may cause responses in a very broad frequency domain so as to hardly maintain the reflector accuracy.

By contrast, Model 1 with drag springs has a totally different dynamic property. The drag springs connect every adjacent two petals together and provide the circumferential tensions to make petals collaborative work. In view of structural dynamics, the drag springs provide the reflector with extra tension stiffness to improve the natural frequencies. The connection of drag springs brings about the multi-petal vibration mode so as to narrow down its frequency domain. It can help to effectively conduct vibration isolation measures to improve the reflector accuracy.

5.2. Effect of Drag Spring Stiffness

In order to explore the quantitative effect, the models with drag spring stiffness S as 40 N/m, 4.0 N/m, 0.4 N/m, 4×10^{-4} N/m, and 4×10^{-7} N/m are computed to investigate the influence of different levels of drag spring stiffness on the vibration natural frequencies of reflector structure. The analysis results are shown in Table 6.

Table 6. Natural frequencies (Hz) of Mode 3, 4, 1, 5, and 6.

Frequency Order	Model 3 $S = 40 \text{ N/m}$	Model 4 $S = 4.0 \text{ N/m}$	Model 1 $S = 0.4 \text{ N/m}$	Model 5 $S = 4 \times 10^{-4} \text{ N/m}$	Model 6 $S = 4 \times 10^{-7} \text{ N/m}$
1	0.9256	0.8290	0.7847	0.7496	0.7494
2	1.0139	0.9009	0.8301	0.7500	0.7495
3	1.6613	1.0934	0.8533	0.7705	0.7704
4	1.6889	1.1296	0.8819	0.7820	0.7818
5	2.4792	1.3610	0.9268	0.7990	0.7989
6	2.5731	1.5566	0.9858	0.8090	0.8087
7	3.1160	1.6749	1.0077	0.8121	0.8120
8	3.2852	1.8324	1.0359	0.8650	0.8648
9	3.4908	1.8618	1.0896	0.8749	0.8744
10	3.7181	2.0415	1.1364	0.8816	0.8815

It is obviously stated that the natural frequencies enlarge with the increase of drag spring stiffness. It is worth noting that there is no difference of natural frequencies between Model 5 and 6. It means

that the natural frequencies of Model 6 with drag spring stiffness $S = 4 \times 10^{-7}$ N/m can be treated as the lower limit of this PDSR with drag springs. This lower limit of structural dynamic property is better than the model without drag springs. It is inferred that the existence of drag springs with pre-tensioned force 3.5 N can substantially change the dynamic property of this reflector structure even though the stiffness tends to zero.

When the stiffness becomes larger, the dispersion of first ten natural frequencies also gets bigger, especially in Model 3. It is indicated that the excessive stiffness of drag springs may apparently affect the stiffness distribution of petals and drag springs. The proportion of drag spring and petal stiffness is the important factor to decide the degree of collaborative work in adjacent petals as shown in Figure 7a. Thus, the moderate stiffness as $S = 0.4$ N/m in Model 1 is feasible for improve the dynamic property of this reflector structure.

5.3. Effect of Drag Spring Pre-Tension Force

Another parameter of drag springs is the pre-tensioned force P. The models with different pre-tensioned force P of drag springs as 3.5 N, 3.0 N, 2.5 N, 2.0 N, and 0.0 N are analyzed to study the influence on the structural dynamics of this reflector. The natural frequencies of each model are listed in Table 7.

Table 7. Natural frequencies (Hz) of Mode 1, 7, 8, 9, and 10.

Frequency Order	Model 1 P = 3.5 N	Model 7 P = 3.0 N	Model 8 P = 2.5 N	Model 9 P = 2.0 N	Model 10 P = 0.0 N
1	0.7847	0.7457	0.7022	0.6533	0.3647
2	0.8301	0.7846	0.7360	0.6833	0.3926
3	0.8533	0.8092	0.7621	0.7113	0.4123
4	0.8819	0.8329	0.7802	0.7232	0.4223
5	0.9268	0.8766	0.8233	0.7664	0.4650
6	0.9858	0.9309	0.8722	0.8092	0.5091
7	1.0077	0.9593	0.9081	0.8536	0.5848
8	1.0359	0.9961	0.9558	0.9145	0.6007
9	1.0896	1.0400	0.9870	0.9301	0.6461
10	1.1364	1.0780	1.0159	0.9491	0.7251

The decrease of natural frequencies is comparatively small with reducing pre-tensioned force. When the pre-tensioned force is set as $P = 0.0$ N in Model 10, the first frequency 0.3647 Hz is almost close to the first frequency 0.3331 Hz of Model 2 without the drag springs. But the frequency domain of Model 10 is much narrower than Model 1. It is indicated from another perspective that the existence of drag springs can develop the integrity of structural dynamics with extra drag spring stiffness. Moreover, the pre-tensioned force supplies the structure with the stress stiffness to further improve the whole structural stiffness.

Hence, the function of drag spring stiffness is mainly to develop the structure integrity and narrow down the frequency domain. The function of pre-tensioned force is to totally improve the structure stiffness by extra stress stiffness. However, the pre-tensioned force in drag springs also acts as a driving force during the deployment [13]. Thus, the pre-tensioned force should be controlled at a feasible value as $P = 3.5$ N. The excessive pre-tensioned force may destroy the stability of deploying process.

5.4. Effect of Distance of Linkage Butts

At the same time, it is necessary to investigate the influence of the distance between the adjacent linkage butts on the natural frequencies of reflector structure. Three models based on different distance L of linkage butt design are carried out and the results are shown in Table 8.

Table 8. Natural frequencies (Hz) of Mode 1, 15, and 16.

Frequency Order	Model 1 L = 40 mm	Model 15 L = 80 mm	Model 16 L = 150 mm
1	0.7847	0.7521	0.6500
2	0.8301	0.7803	0.6639
3	0.8533	0.7943	0.6779
4	0.8819	0.8085	0.6785
5	0.9268	0.8354	0.6929
6	0.9858	0.8819	0.7287
7	1.0077	0.8980	0.7588
8	1.0359	0.9093	0.7827
9	1.0896	0.9507	0.7845
10	1.1364	1.0373	0.8706

According to the results of three levels of linkage butt distance L , there is an approximately linear variation trend between the natural frequencies and linkage butt distance L . With the enlargement of linkage butt distance L , this downward trend of natural frequencies decreases slowly. The longer the distance between two adjacent linkage butts is, the more flexible the drag spring becomes. It is demonstrated that the linkage butts should be set on the boundary of the petal for model design.

6. Conclusions

In this paper, the Petal-type Deployable Solid-surface Reflector was researched from a perspective of its structural dynamic properties. The Cable Replacement Method was utilized to equivalently simulate the nonlinear structural stiffness of the revolute joint for numerical analyses. The FEMs of this reflector structure were established on the basis of ANSYS and verified by the theoretical analysis and dynamic test of actual prototype model. The natural frequencies and mode shapes of deployed reflector were computed to study the influence of drag spring design parameters as stiffness, pre-tensioned force, and distance of two adjacent linkage butts. The results were concluded as following.

(1) The existence of drag springs radically changes the structural style for this reflector to largely improve the natural frequencies. It brings about the multi-petal vibration mode to narrow down the frequency domain.

(2) The function of drag spring stiffness is mainly to develop the structure integrity and narrow down the frequency domain. The function of pre-tensioned force is to totally improve the structure stiffness by extra stress stiffness.

(3) The distance between two adjacent linkage butts also decides the rigidity of drag springs, and the linkage butts should be set on the boundary of the petal for model design.

(4) By means of setting up drag springs with these parameters, the dynamic properties of reflector structure can be improved to enhance the structural stiffness for natural frequencies and narrow down the frequency domain, which is effectively helpful in vibration isolation measures for reflector accuracy development.

The drag springs between two adjacent petals can essentially improve the dynamic performance of reflector structure in deployed state. This conclusion can be a useful technical system for future engineering applications of the PDSR antenna.

In summary, the CRM has been verified to effectively simulate the dynamic property of the structure with revolute joints. The simulation of the revolute joint locked by the torsion spring and rotation limiter can be modeled by the cable element to reflect the sudden change of the stiffness on clockwise and counterclockwise rotation. Thus, it is accurate to reflect the rotation DOF and define its stiffness for the revolute joint. Another advantage is that this method can be widely applied in the numerical simulations of deployable structures based on its efficiency. However, this method should be further explored by theoretical method to develop the accuracy for the stiffness definition of the real

revolute joint. Future works will focus on theoretical research of structure dynamics with revolute joints and deeply experimental studies on this reflector model and the CRM.

Author Contributions: Conceptualization, H.H.; methodology, H.H.; investigation, Q.C. and L.Z.; model analysis, Q.C.; test, L.Z. and Q.C.; validation, H.H.; writing—original draft preparation, Q.C. and H.H.; writing—review and editing, H.H. All authors have read and agreed to the published version of the manuscript.

Funding: This research is supported by the National Natural Science Foundation of China (Grant No. 11902253) and the Fundamental Research Funds for the Central Universities of China. The authors are grateful for this support.

Conflicts of Interest: The authors declare that there is no conflict of interest. The funders had no role in the design of the study; in the collection, analyses, or interpretation of data; in the writing of the manuscript, or in the decision to publish the results.

References

1. Li, T.; Ma, X. Technologies of large deployable space antennas. *Space Electron. Technol.* **2012**, *9*, 35–39.
2. Liu, R.; Tian, D.; Deng, Z. Research actuality and prospect of structure for space deployable antenna. *J. Mach. Des.* **2010**, *27*, 1–10.
3. Liu, R.; Shi, C.; Guo, H.; Li, B.; Tian, D.; Deng, Z. Review of space deployable antenna mechanisms. *J. Mech. Eng.* **2020**, *56*, 1–12.
4. Im, E.; Thomson, M.; Fang, H.; Pearson, J.; Moore, J.; Lin, J. Prospects of large deployable reflector antennas for a new generation of geostationary Doppler weather radar satellites. In Proceedings of the AIAA, SPACE 2007 Conference & Exposition, Long Beach, CA, USA, 18–20 September 2007; pp. 1–17.
5. Semler, D.; Tulintseff, A.; Sorrell, R.; Marshburn, J. Design, integration and deployment of the terreStar 18-meter reflector. In Proceedings of the AIAA, 28th International Communications Satellite Systems Conference (ICSSC-2010), Anaheim, CA, USA, 30 August–2 September 2010; p. 8855.
6. Bartsch, A.; Trofaiar, A.M.; Hayman, G.; Sabel, D.; Schlaffer, S.; Clark, D.B.; Blyth, E. Detection of open water dynamics with ENVISAT ASAR in support of land surface modelling at high latitudes. *Biogeosciences* **2012**, *9*, 703–714. [[CrossRef](#)]
7. Kardashev, N.S.; Khartov, V.V.; Yakimov, V.E. “RadioAstron”—A telescope with a size of 300000 km: Main parameters and first observational results. *Astron. Rep.* **2013**, *57*, 153–194. [[CrossRef](#)]
8. Hu, F.; Song, Y.; Zheng, S.; Huang, Z.R.; Zhu, J. Advances and trends in space truss deployable antennae. *J. Astronaut.* **2018**, *39*, 111–120.
9. Hoang, B.; Spence, B.; White, S.; Spence, B.; Kiefer, S. Commercialization of deployable space systems’ roll-out solar array (ROSA) technology for Space Systems Loral (SSL) solar arrays. In Proceedings of the 2016 IEEE Aerospace Conference, Big Sky, MT, USA, 5–12 March 2016.
10. Li, H.; Liu, X.; Guo, S.; Cai, G.P. Deployment dynamics and control of large-scale flexible solar array system with deployable mast. *Adv. Space Res.* **2016**, *58*, 1288–1302. [[CrossRef](#)]
11. Hanayama, E.; Kuroda, S.; Takano, T.; Kobayashi, H.; Kawaguchi, N. Characteristics of the large deployable antenna on HALCA satellite in orbit. *IEEE Trans. Antennas Propag.* **2004**, *52*, 1777–1782. [[CrossRef](#)]
12. Brown, M.A. Deployable mast for solar sails in the range of 100–1000m. *Adv. Space Res.* **2011**, *48*, 1747–1753. [[CrossRef](#)]
13. Huang, H.; Guan, F.L.; Pan, L.L.; Xu, Y. Design and deploying study of a new petal-type deployable solid surface antenna. *Acta Astronautica* **2018**, *148*, 99–110. [[CrossRef](#)]
14. Hu, H.; Tian, Q.; Zhang, W.; Jin, D.P.; Hu, G.K.; Song, Y.P. Nonlinear dynamics and control of large deployable space structures composed of trusses and meshes. *Adv. Mech.* **2013**, *43*, 390–414.
15. Dai, L.; Guan, F.; Guest, J. Structural optimization and model fabrication of a double-ring deployable antenna truss. *Acta Astronautica* **2014**, *94*, 843–851. [[CrossRef](#)]
16. Yan, S.; Chen, L.; Wu, D.; Jin, D.-W. Experimental studies of behavior of nonlinear dynamics of a deployable structure for spacecraft. *J. Astronaut.* **2002**, *23*, 1–3.
17. Guo, H.; Zhang, J.; Liu, R.; Deng, Z. Effects of joint on dynamics of space deployable structure. *Chin. J. Mech. Eng.* **2013**, *26*, 861–872. [[CrossRef](#)]
18. Weeks, G.E. Dynamic analysis of a deployable space structure. *J. Spacecr. Rocket.* **1986**, *23*, 102–107. [[CrossRef](#)]

19. Li, T.; Guo, J.; Cao, Y. Dynamic characteristics analysis of deployable space structures considering joint clearance. *Acta Astronautica* **2011**, *68*, 974–983. [[CrossRef](#)]
20. Liu, R.; Guo, H.; Liu, R.; Wang, H.; Tang, D.; Deng, Z. Structural design and optimization of large cable-rib tension deployable antenna structure with dynamic constraint. *Acta Astronautica* **2018**, *151*, 160–172. [[CrossRef](#)]
21. Wild, W.; Baryshev, A.; de Graauw, T.; Kardashev, N.; Likhachev, S.; Goltsman, G.; Koshelets, V. Instrumentation for Millimetron—A large space antenna for THz astronomy. In Proceedings of the International Symposium on Space Terahertz Technology, Groningen, The Netherlands, 28–30 April 2008; pp. 186–191.
22. Lee, J.Y.; Yoon, S.S.; Kim, S.H.; Lee, T.K.; Lee, J.W.; Roh, J.H.; Yi, D.W. Performance of solid surface deployable antenna for panel misalignment. In Proceedings of the 2016 URSI Asia-Pacific Radio Science Conference, Seoul, Korea, 21–25 August 2016; pp. 877–879.
23. Bujakas, V.I. New Design of Petal Type Deployable Space Mirror. *Multibody Mechatron. Syst.* **2015**, *25*, 391–398.
24. Schwarz, S.; Barho, R. Deployment mechanisms for a 5m unfurlable reflector. In Proceedings of the European Space Mechanisms and Tribology Symposium, Munich, Germany, 18–20 September 2019.
25. Huang, H.; Guan, F. Mechanical study on initial profile solution for inflatable reflector made of orthotropic material. *Acta Astronautica* **2014**, *104*, 179–185. [[CrossRef](#)]
26. Huang, H.; Guan, F. Sensitivity Study on Optimizing Thickness Distribution for a Membrane Reflector. *Int. J. Aerosp. Eng.* **2019**, *2019*. [[CrossRef](#)]
27. Zhu, S. Design and Test of Deployable Plane Structure for Spaceborne Platform. Master's Thesis, Zhejiang University, Zhejiang, China, 2015.
28. Clough, R.W.; Penzien, J. *Dynamic of Structures*, 3rd ed.; Computers & Structures, Inc.: Berkeley, CA, USA, 2003.
29. Jiangsu Donghua Test Technology Co. Ltd. *Structural Mode Test. Analysis System Scheme*; Technical Report No. DHC/J0.6-28; Jiangsu Donghua Test Technology Co. Ltd.: Jiangsu, China, 2020.



© 2020 by the authors. Licensee MDPI, Basel, Switzerland. This article is an open access article distributed under the terms and conditions of the Creative Commons Attribution (CC BY) license (<http://creativecommons.org/licenses/by/4.0/>).